

Dissipationless Mergers of Elliptical Galaxies and the Evolution of the Fundamental Plane

Michael Boylan–Kolchin^{1*}, Chung–Pei Ma^{2†}, and Eliot Quataert^{2‡}

¹*Department of Physics, University of California, Berkeley, CA 94720, USA*

²*Department of Astronomy, University of California, Berkeley, CA, 94720, USA*

23 September 2018

ABSTRACT

We carry out numerical simulations of dissipationless major mergers of elliptical galaxies using initial galaxy models that consist of a dark matter halo and a stellar bulge with properties consistent with the observed fundamental plane. By varying the density profile of the dark matter halo (standard NFW versus adiabatically contracted NFW), the global stellar to dark matter mass ratio, and the orbit of the merging galaxies, we are able to assess the impact of each of these factors on the structure of the merger remnant. Our results indicate that the properties of the remnant bulge depend primarily on the angular momentum and energy of the orbit; for a cosmologically motivated orbit, the effective radius and velocity dispersion of the remnant bulge remain approximately on the fundamental plane. This indicates that the observed properties of elliptical galaxies are consistent with significant growth via late dissipationless mergers. We also find that the dark matter fraction within the effective radius of our remnants increases after the merger, consistent with the hypothesis that the tilt of the fundamental plane from the virial theorem is due to a varying dark matter fraction as a function of galaxy mass.

Key words: galaxies: fundamental parameters – galaxies: structure – galaxies: evolution – dark matter – methods: N -body simulations

1 INTRODUCTION

Galaxy merging is thought to be the dominant process in the formation and evolution of elliptical galaxies (e.g., Toomre & Toomre 1972). This picture is broadly supported by both observations and simulations and fits naturally into the Λ CDM hierarchical cosmology (e.g., Steinmetz & Navarro 2002). Much, however, remains to be understood about the gas and stellar dynamics during mergers. For example, recent simulations indicate that not all mergers of gas-rich spiral galaxies result in a bulge-dominated remnant (Springel & Hernquist 2005).

Although gas-rich starbursts may form many of the stars contained in elliptical galaxies, it is also likely that stars are later assembled into larger remnants via nearly dissipationless mergers, particularly during the formation of groups and clusters (Gao et al. 2004). There is in fact direct observational evidence for “red” mergers (lacking significant star formation), both in local observations with the Sloan Digital Sky Survey (SDSS; Masjedi and Hogg, private com-

munication) and in a luminous X-ray cluster at $z = 0.83$ (van Dokkum et al. 1999). In addition, the semi-analytic study of Khochfar & Burkert (2003) found that the most recent merger of a luminous elliptical galaxy ($M_B \lesssim -21$) is likely to have been between two bulge-dominated galaxies rather than two gas-rich spirals, again pointing to the importance of dissipationless merging for the evolution of elliptical galaxies.

Observationally, early type galaxies exhibit a well-defined correlation among their effective radii R_e , luminosities L (or equivalently surface brightness $I \propto L/R_e^2$), and central velocity dispersions σ . This “fundamental plane” (Djorgovski & Davis 1987; Dressler et al. 1987) is often expressed as

$$R_e \propto \sigma^a I^b \quad (1)$$

and has been measured by many groups with varying results. For example, Jorgensen, Franx, & Kjaergaard (1996) measured $a = 1.24 \pm 0.07$ and $b = -0.82 \pm 0.02$ from a set of 225 early-type galaxies in nearby clusters observed in the r-band. This is consistent with the original observations by Djorgovski & Davis (1987) and Dressler et al. (1987) but noticeably different from the SDSS determination (based on ~ 9000 early-type galaxies) of $a =$

* E-mail: mrbk@astro.berkeley.edu

† E-mail: cpma@astro.berkeley.edu

‡ E-mail: eliot@astro.berkeley.edu

1.49 ± 0.05 and $b = -0.75 \pm 0.01$ (Bernardi et al. 2003b), values more similar to the K-band fundamental plane of Pahre, de Carvalho, & Djorgovski (1998). The reason for this discrepancy is not currently clear.

Projections of the fundamental plane are also of interest in studies of galaxy evolution. The SDSS team measured a radius-luminosity relation of

$$R_e \propto L^{0.63 \pm 0.025} \quad (2)$$

and a Faber–Jackson (1976) relation of

$$\sigma \propto L^{0.25 \pm 0.012} \quad (3)$$

(Bernardi et al. 2003a), while work by Kauffmann et al. (2003) on the stellar mass content of SDSS galaxies allowed Shen et al. (2003) to determine the scaling of effective radius with stellar mass:

$$R_e \propto M_*^{0.56}. \quad (4)$$

The fundamental plane has typically been interpreted as a manifestation of the virial theorem, which relates σ and R to the *total* enclosed (dynamical) mass M_{dyn} and predicts a correlation in the fundamental properties of galaxies:

$$\sigma^2 \propto \frac{M_{dyn}}{R} = \left(\frac{M_{dyn}}{L} \right) \left(\frac{L}{R^2} \right) R \propto \left(\frac{M_{dyn}}{L} \right) IR, \quad (5)$$

giving the relation

$$R \propto \sigma^2 I^{-1} \left(\frac{M_{dyn}}{L} \right)^{-1}. \quad (6)$$

Clearly this virial theorem expectation is incompatible with the observed fundamental plane in equation (1) if light traces the dynamical mass ($M_{dyn} \propto L$). A systematic variation of M_{dyn}/L with luminosity is usually assumed to “tilt” the virial theorem scalings into the observed ones. Since

$$\frac{M_{dyn}}{L} = \left(\frac{M_{dyn}}{M_*} \right) \left(\frac{M_*}{L} \right), \quad (7)$$

this tilt could result from increasing M_*/L with L due to, for instance, varying metallicity or stellar population age, or from increasing M_{dyn}/M_* with L due to higher dark matter fraction in the central parts of more luminous galaxies. Conflicting conclusions have been reported in the literature as to which of these explanations is correct (for instance, compare Gerhard et al. 2001 with Padmanabhan et al. 2004). Structural or dynamical non-homology could also contribute to the fundamental plane tilt (e.g., Capelato, de Carvalho, & Carlberg 1995; Graham & Colless 1997; Pahre, de Carvalho, & Djorgovski 1998).

Numerical simulations are a powerful way to assess the dynamics of galaxy mergers. There is a substantial body of work devoted to simulations of mergers of galaxies in the context of forming ellipticals (for reviews, see Barnes & Hernquist 1992 and Burkert & Naab 2003). Several studies have in particular addressed the question of whether collisionless mergers of galaxies preserve the fundamental plane relations. These studies typically used simulations of $\sim 10^4$ particles (per initial galaxy) and have reached varying and sometimes conflicting results. For instance, González-García & van Albada (2003) studied mergers of one-component systems (stellar bulges without dark matter haloes) with $R_e \propto M^{0.5}$ and found that the merger remnants ended up very near the fundamental plane defined

by the progenitors. Dantas et al. (2003) found that mergers of bulge-only galaxies remained on the fundamental plane, while mergers of galaxies containing both bulge and dark matter components produced a fundamental plane with a tilt larger than that observed. Nipoti, Londrillo, & Ciotti (2003) used repeated mergers of one- and two-component galaxies to follow the merging process over a large range in mass. They found that neither the $R_e - M_*$ nor the $M_* - \sigma_e$ relation was preserved in their dissipationless mergers but the full fundamental plane of their merger remnants agreed with observations.

In this paper we carry out dissipationless mergers of early type galaxies, focusing on major mergers of two-component (dark matter plus stellar bulge) systems. We thus do not address the origin of either bulge-dominated galaxies or the fundamental plane but rather investigate whether dissipationless mergers maintain the tight fundamental plane relations, a scenario that is likely important for massive ellipticals. We pay particular attention to using cosmologically motivated models that include adiabatic contraction of dark matter haloes and merger orbits drawn from cosmological simulations. We also use a significantly larger number of simulation particles than many previous studies, which is necessary to avoid spurious two-body relaxation (and an accompanying artificial expansion of the stellar bulge). In the next section, we describe our initial models and choice of simulation parameters in more detail. Section 3 discusses properties of both the stellar and dark matter components of the merger remnants in our simulations, including their radial density profiles, triaxiality, if and how the fundamental plane scalings and structural homology are preserved, and the changes in the mass ratio M_{dyn}/M_* in the inner parts of the remnants. Section 4 includes a discussion and summary of our results.

2 SIMULATIONS

2.1 Galaxy Models and Initial Conditions

Our model galaxies consist of two components, a stellar bulge and a dark matter halo. We model the initial spatial distribution of the bulge with a Hernquist (1990) density profile,

$$\rho_*(r) = \frac{M_*}{2\pi a^3} \frac{1}{r/a} \left(\frac{1}{1+r/a} \right)^3 \quad (8)$$

with total stellar mass M_* , quarter-mass radius $r_{1/4} = a$, and half-mass radius $r_{1/2} = (1 + \sqrt{2})a$. Observationally, a useful radius is the effective radius R_e , defined as the radius of the isophote that encloses half of the total (projected) stellar luminosity. For equation (8), the effective radius is related to the quarter- and half-mass radii by $R_e = 1.8153a = 0.752r_{1/2}$. The Hernquist profile in projection follows the de Vaucouleurs (1948) $r^{1/4}$ law to within 35% in the radial range $0.06 \leq R/R_e \leq 14.5$ (Hernquist 1990), a region containing over 90% of the model’s total luminosity.

For the dark matter component, we consider two possible radial density profiles: the NFW profile (Navarro, Frenk, & White 1997) and a more realistic

version of this profile that uses the adiabatic contraction approximation (Blumenthal et al. 1986) to model the response of the dark matter halo to baryons. The uncompressed NFW profile is given by

$$\rho_{dm}(r) = \frac{\rho_c \delta_c}{(cr/r_v)(1 + cr/r_v)^2}, \quad (9)$$

where the concentration parameter c is defined as the ratio of the virial radius r_v to the radius at which the logarithmic slope of the density profile equals -2 (also known as the scale radius r_s). The additional parameter δ_c depends on c and the choice of virial overdensity Δ_v relative to the critical density ρ_c :

$$\delta_c = \frac{\Delta_v c^3}{3[\ln(1+c) - c/(1+c)]}. \quad (10)$$

We use $\Delta_v = 200$ throughout this paper. Since equation (9) is logarithmically divergent as $r \rightarrow \infty$, we use the exponential truncation scheme described by Springel & White (1999) for our haloes at $r > r_v$. Truncating the haloes in this manner requires $\approx 10\%$ more simulation particles than a sharp truncation at the virial radius but keeps the outer part of the halo in equilibrium.

We calculate the adiabatically compressed dark matter density profile from the initial (NFW) dark matter profile and the final baryon (Hernquist) profile under the assumptions of homologous contraction, circular orbits for the particles, and conservation of angular momentum $rM(<r)$:

$$r_i [M_b(r_i) + M_{dm}(r_i)] = r_f [M_b(r_f) + M_{dm}(r_i)]. \quad (11)$$

Although it is not obvious that the adiabatic contraction approximation should be directly applicable to elliptical galaxies – it was originally proposed to describe the response of a dark matter halo to baryonic dissipation during disk formation – simulations have shown it to be surprisingly accurate for modeling ellipticals. Recent hydrodynamical simulations (Gnedin et al. 2004) find that equation (11) overpredicts the amount of contraction at small radii but this difference is much smaller than the difference between haloes with and without adiabatic contraction, so we do not expect it to significantly affect our results.

Fig. 1 shows the initial density profiles (top panel) and 1-d velocity dispersions (bottom panel) of the stellar bulge (symbols) and dark matter haloes (plain curves) in our simulations. It also illustrates the effects of compression in the dark matter haloes (solid vs dashed curves). The top panel shows that the mass density interior to $R_e = 2.8$ kpc is dominated by the stellar component when the dark matter halo follows the NFW profile without compression, but compression increases the central dark matter density significantly and raises it to be larger than the stellar density at $r \gtrsim 1$ kpc. Compression also steepens the NFW $\rho \propto r^{-1}$ density cusp to nearly isothermal (r^{-2}) at $r \gtrsim 1$ kpc (although the compressed density still asymptotes to r^{-1} at very small r). The bottom panel shows that adiabatic compression increases the velocity dispersion of both the dark matter and stellar components. It is also interesting to note that regardless of compression, the mere presence of a stellar bulge in a dark matter halo increases the velocity dispersion of the dark matter component by up to a factor of ~ 2 (for $r > 1$ kpc) in comparison with that of an NFW halo without a bulge (dotted curve). This effect also greatly reduces the ra-

dius at which the “temperature inversion” characteristic of the NFW profile occurs.

We construct the N -Body models by setting the bulge and dark matter halo to be in equilibrium in the total gravitational potential. We assume that each component is both spherical and isotropic. The particle positions for each component are initialized from the density profile of that component. The particle velocities are drawn based on each component’s equilibrium distribution function $f_i(E)$, which we calculate numerically using Eddington’s formula (Binney & Tremaine 1987):

$$f_i(E) = \frac{1}{\sqrt{8\pi^2}} \int_0^E \frac{d^2 \rho_i}{d\psi^2} \frac{d\psi}{\sqrt{E-\psi}}, \quad (12)$$

where ρ_i is the density profile of component i while ψ is the *total* gravitational potential. (This is to be contrasted with the typical one-component model, where ρ and ψ are related by Poisson’s equation.) This method of selecting the velocities is self-consistent and makes no assumptions about the local form of the velocity distribution, allowing us to create stable initial conditions (see Kazantzidis, Magorrian, & Moore (2004) for a full discussion of sampling velocities when constructing initial conditions for N-body models). Note that while the *positions* of the particles in each component are the same as would be given in a one-component model, the *velocities* are not due to the presence of the other component.

2.2 Model Parameters and Merger Orbits

Table 1 summarizes the parameters used in the galaxy models and simulations for our series of production and test runs. Before adiabatic compression, the initial haloes in our simulations have $M_{dm} = 10^{12} M_\odot$ and concentration $c = 10$, giving a scale radius of $r_s = 16.26$ kpc and virial radius of $r_v = 162.6$ kpc. Gravity is the only physics in our simulation, meaning we can in principle interpret the results at different mass scales by a corresponding scaling of time and length. In practice, however, the presence of a stellar bulge complicates this scaling (see Section 4 for details). We consider two values for the total dark matter to stellar mass ratios, $M_{dm}/M_* = 20$ ($M_* = 5 \times 10^{10} M_\odot$) and $M_{dm}/M_* = 10$ ($M_* = 10^{11} M_\odot$), which are chosen to be representative of the values estimated from SDSS (Padmanabhan et al. 2004) and weak lensing (Seljak 2002). As discussed in Section 3, we do not find the merger remnants to depend sensitively on this ratio. We relate the remaining free parameter of the Hernquist density profile – the length scale R_e – to the stellar mass using the observed $R_e - M_*$ relation of early-type galaxies in SDSS (Shen et al. 2003)¹:

$$R_e = 4.16 \left(\frac{M_*}{10^{11} M_\odot} \right)^{0.56} \text{ kpc} \quad (13)$$

Our choices of M_{dm}/M_* and R_e do not guarantee that the velocity dispersion σ_e of a model bulge will lie on the observed fundamental plane. In fact, observations of the fundamental plane measure the Faber-Jackson $L - \sigma_e$ relation

¹ Note the correct coefficient in Table 1 of Shen et al. (2003) is 2.88×10^{-6} rather than 3.47×10^{-5} (S. Shen, private communication)

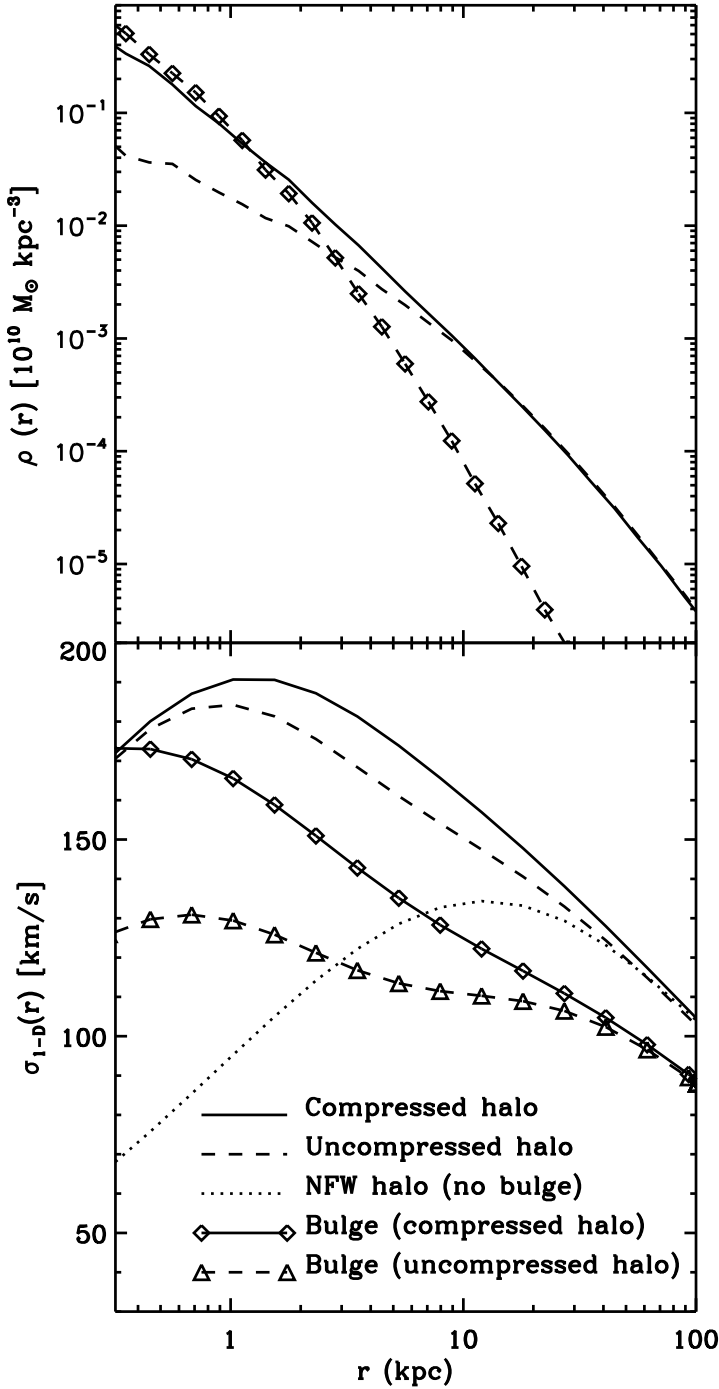


Figure 1. Initial radial density profiles $\rho(r)$ (top) and 1-d velocity dispersion profiles $\sigma(r)$ (bottom) of the stellar bulge (symbols) and dark matter halo (plain curves) used in our simulations. The dark matter and bulge masses are set to be $M_{dm} = 10^{12} M_\odot$ and $M_* = M_{dm}/20$ here. An adiabatically compressed dark matter halo (solid) has a larger ρ and σ than the standard NFW halo (dashed) in the inner tens of kpc. The velocity profile of a standard bulge-less NFW halo of the same mass is plotted (dotted curve) for comparison. (The density profile of the bulge-less NFW halo is the same as the uncompressed NFW halo).

while our simulations use the $M_* - \sigma_e$ relation. We relate the two using the r^* band values from SDSS (Bernardi et al. 2003a). Assuming $M_*/L = 3 - 3.5$ in the r^* band, consistent with the estimates of Kauffmann et al. (2003), we find that a bulge of $M_* = 5 \times 10^{10} M_\odot$ should have a characteristic velocity dispersion of ~ 160 km/s. Table 1 shows that this is reasonably consistent with the values we obtain from model M20 (which includes adiabatic contraction) and is noticeably higher than the uncompressed halo model (M20u). In order to lie on the $M_* - \sigma_e$ relation, the uncompressed model must have a very large value of $M_*/L \sim 8$. Adiabatic contraction (and the associated increase in the dark matter fraction at small radii) therefore helps put the initial galaxy models closer to the observed fundamental plane (see, however, Borriello, Salucci, & Danese 2003 for an alternate view).

In addition to the internal structure of the bulge and dark matter halo, the orbit of a binary encounter is also important in determining the properties of the merger remnants. For instance, it is well-known that radial orbits tend to result in prolate remnants whereas orbits with significant angular momentum generally give oblate or triaxial end-products (Moore et al. 2004 and references therein). Most merger studies to date have assumed parabolic orbits with somewhat ad hoc impact parameters. We attempt to use more realistic orbits by drawing from recent results on the orbital distribution of merging dark matter haloes in cosmological N-Body simulations.

Benson (2005), for example, has analyzed the orbital parameters of minor mergers in the Virgo Consortium’s N-Body simulations of a Λ CDM model.² He finds that the orbital distribution peaks at semi-major axis $\approx r_v$ and eccentricity e slightly less than 1. Khochfar & Burkert (2005) studied similar quantities in major mergers (with mass ratio within 4:1) and found that the distribution of circularities peaks at $\epsilon = \sqrt{1 - e^2} = 0.5$, consistent with the findings of Benson, an earlier study by Tormen (1997), and recent results from Zentner et al. (2005). We therefore choose a “most probable” orbit defined by $\epsilon = 0.5$ and pericentric distance $r_p = 50$ kpc, consistent with Khochfar & Burkert’s relation $r_p = 210\epsilon^{2.07}$ kpc. We assign the radial and tangential velocities v_r and v_θ of this orbit to agree with Benson’s analysis (his Figs. 2 & 7, and equation 2): $v_r = v_{vir}$ and $v_\theta = 0.7v_{vir}$ where $v_{vir}^2 = GM_{vir}/R_{vir}$. In addition to the “most probable” orbit, we also simulate a head-on parabolic merger for comparison. Finally, we perform one modified “most probable” simulation in which both v_r and v_θ are reduced by 15% in order to test how robust our results are to the choice of initial orbital velocities. The initial center-of-mass velocity for each run is listed in Table 1. In all cases we start with the galaxy centers separated by two virial radii.

2.3 Simulations and Resolution Studies

We use **GADGET** (Springel, Yoshida, & White 2001), an efficient parallelized tree code, to perform the simulations presented below. We set the force softening $\epsilon = 0.3$ kpc for both star and dark matter particles; this choice corresponds to either $0.072R_e$ ($M_* = 10^{11} M_\odot$) or $0.11R_e$ ($M_* = 5 \times 10^{10} M_\odot$)

² <http://www.mpa-garching.mpg.de/Virgo/>

Table 1. Simulation and model parameters of each galaxy in the initial conditions used in our production runs (upper 5) and test runs. In the run names, the merger orbits are distinguished by “M” and “R” for “most probable” vs. radial (parabolic) orbits; the mass fraction M_{dm}/M_* is labeled by 20 vs. 10; the runs with initially uncompressed dark matter halos are denoted by “u”. Run N20 is identical to run M20 except the magnitude of each component of the initial orbital velocity is reduced by 15%. N_{dm} and N_* are the numbers of dark matter and stellar particles used in each simulation. All dark matter halos have virial masses of $10^{12} M_\odot$ and virial radii of 162.6 kpc.

| Run | $\frac{M_{dm}}{M_*}$ | N_{dm} | N_* | R_e^a | σ_e^b | v_{CM}^c |
|--------|----------------------|-------------------|-------|---------|--------------|------------|
| M10 | 10 | 5.5×10^5 | 49000 | 4.13 | 173.5 | 200 |
| M20 | 20 | 5.5×10^5 | 24500 | 2.85 | 151.4 | 200 |
| N20 | 20 | 5.5×10^5 | 24500 | 2.85 | 151.4 | 170 |
| M20u | 20 | 5.5×10^5 | 24500 | 2.83 | 122.7 | 200 |
| R20 | 20 | 5.5×10^5 | 24500 | 2.83 | 150.4 | 250 |
| M10t1 | 10 | 1.1×10^5 | 49000 | 4.13 | 172.8 | 200 |
| M20t0 | 20 | 1.1×10^5 | 4900 | 2.79 | 151.3 | 200 |
| M20t1 | 20 | 1.1×10^5 | 24500 | 2.76 | 150.9 | 200 |
| M20t2 | 20 | 1.1×10^5 | 49000 | 2.80 | 150.1 | 200 |
| M20t1u | 20 | 1.1×10^5 | 24500 | 2.76 | 123.1 | 200 |
| R20t1 | 20 | 1.1×10^5 | 24500 | 2.76 | 150.9 | 250 |

^aeffective radius of stellar bulge, in kpc

^baperture velocity dispersion of stellar bulge (eq. 15), in km s^{-1}

^ccenter-of-mass velocity for merger, in km s^{-1}

for our initial galaxy models. We run each model until the remnant reached virial equilibrium (between 4 and 6 Gyr depending on the orbit). Energy is conserved to within 0.5% for all runs and the global virial ratio $2T/|W|$ is unity to within 1.5% at the final timestep in each case.

We have performed several convergence tests to ensure that sufficient particle numbers and force resolution are used for both the dark matter and stellar components. We find that increasing the number of star particles N_* from 24500 to 49000 (runs M20t1 and M20t2) at fixed dark matter particle number does not affect our results for R_e and σ_e . It is, however, important to use $N_{dm} \approx 5 \times 10^5$ dark matter particles per halo since our test runs with $N_{dm} \approx 10^5$ show noticeable differences: for example, if we assume $R_e \propto M_*^\alpha$, using $N_{dm} = 10^5$ rather than 5×10^5 causes an overestimation of α at the 15% level (for a compressed halo with $M_{dm}/M_* = 20$). This effect can be understood in terms of two-body relaxation: using a small number of particles means that on small scales, individual particle interactions become important even when compared to the mean gravitational field. This causes an artificial heating, diluting the dark matter potential at the center of the model galaxy, and resulting in an artificially expanded stellar bulge. Similarly the final stellar velocity dispersions in the test runs tend to come out lower than in the production runs, again because of the shallower central potential. This effect leads to an overestimate of R_e and an under-estimate of σ_e , biasing the fundamental plane correlations we hope to measure. As listed in Table 1, our production runs all use 5.5×10^5 dark matter particles and 24500 stellar particles (for $M_{dm}/M_* = 20$). These values provide enough mass resolution in both dark

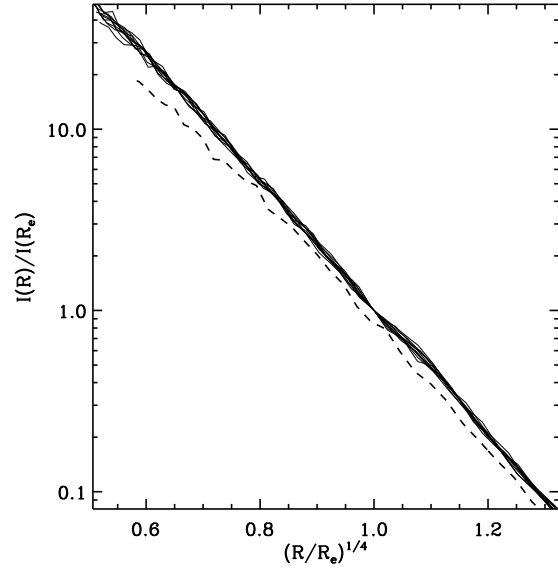


Figure 2. Surface brightness profiles for run M20 at $t=0$ Gyr (dashed curve) and ten random projections at $t=6$ Gyr (solid curves) as a function of $(R/R_e)^{1/4}$ and normalized to unity at $R = R_e$ (the initial profile is offset by 15% for clarity). A de Vaucouleurs law is a straight line on this plot.

and stellar matter to resolve quantities of interest on scales larger than ~ 1 kpc.

3 PROPERTIES OF MERGER REMNANTS

The global merger dynamics in our simulations using the “most probable” orbit is similar in all three cases (runs M10, M20, and M20u). As the galaxies spiral in toward each other, the dense stellar bulges stay intact while the more diffuse dark matter haloes mix rapidly. Dynamical friction then brings the bulges and the central core of the dark matter haloes together and the merger is finished after approximately 5 Gyr. The process for the radial orbit is about 30% faster even though the initial orbit is more unbound because the orbit brings the bulges together earlier. In the following sections we quantify the structure and kinematics of the merger remnants and then discuss the extent to which the merger preserves homology and maintains the fundamental plane relations of elliptical galaxies.

3.1 Surface Brightness and Radial Density Profiles

One distinctive property of the bulges in early-type galaxies is that their surface brightness profiles follow the de Vaucouleurs law, $\log I(R) \propto -R^{1/4}$. Fig. 2 shows $I(R)$ for 10 random projections of the final bulge from run M20 (solid lines) as a function of $(R/R_e)^{1/4}$. For comparison we also show $I(R)$ of the initial bulge (dashed line; offset by 15% for clarity). Each of the random projections of the final bulge, as well as the initial profile, all follow the de Vaucouleurs law over the plotted range of $\epsilon \leq R \leq R_{90}$ (where R_{90} is the projected radius containing 90% of the bulge mass).

Table 2. Fits to the radial density profiles of dark matter haloes and stellar bulges at $t = 0$ and 6 Gyr in our five production runs. Parameters A , B , and C are defined in equation (14). Haloes are fit on the range [1,100] kpc, bulges on the range [0.32,16] kpc.

| Run | time (Gyr) | Dark Matter Haloes | | | | Stellar Bulges | | | |
|------|---------------|--------------------------------|---|--------------|------|--------------------------------|--------------------|--------------|------|
| | | M_v ($10^{10} M_\odot$) | A ($10^5 M_\odot \text{kpc}^{-3}$) | B (kpc) | C | M_* ($10^{10} M_\odot$) | $r_{1/4}$ (kpc) | B (kpc) | C |
| M10 | 0 | 100.6 | 14.8 | 32.5 | 1.8 | 10.1 | 2.24 | 2.19 | 0.97 |
| | 6 | 133.8 | 17.3 | 34.1 | 1.8 | 18.6 | 2.94 | 4.47 | 1.5 |
| M20 | 0 | 100.4 | 9.52 | 39.4 | 1.8 | 5.02 | 1.57 | 1.55 | 0.98 |
| | 6 | 136.8 | 12.1 | 40.2 | 1.8 | 9.75 | 2.26 | 3.83 | 1.6 |
| N20 | 0 | 100.4 | 9.52 | 39.4 | 1.8 | 5.02 | 1.57 | 1.55 | 0.98 |
| | 5.5 | 144.1 | 9.87 | 44.8 | 1.8 | 9.82 | 2.21 | 4.31 | 1.7 |
| M20u | 0 | 100.0 | 134 | 15.8 | 0.98 | 5.08 | 1.56 | 1.68 | 1.1 |
| | 6 | 136.2 | 114 | 18.8 | 1.1 | 9.92 | 2.04 | 3.88 | 1.7 |
| R20 | 0 | 100.4 | 6.84 | 45.2 | 1.8 | 5.06 | 1.56 | 1.55 | 0.99 |
| | 4 | 132.1 | 14.6 | 37.6 | 1.7 | 10.1 | 2.89 | 7.31 | 1.9 |

Although the remnants’ projected density profiles mimic those of the initial conditions, the unprojected density profiles are not necessarily identical. In order to quantify the changes in density structure induced by the merger, we fit both the bulges and dark matter haloes to the following profile:

$$\rho(r) = \frac{A}{(r/B)^C (1 + r/B)^{(D-C)}}. \quad (14)$$

Since we find the outer slopes of both the dark matter haloes and stellar bulges to be mostly unaffected by the merger, we fix D to their initial values: $D = 3$ for the halo and $D = 4$ for the stellar bulge. Models with $D = 4$ have been investigated by Dehnen (1993) and Tremaine et al. (1994); for these it is possible to relate A to B , C , and M_* : $A = (3 - C)M_*/(4\pi B^3)$. Initially the bulges are all described by Hernquist density profiles, so $A = M_*/(2\pi a^3)$, $B = a = r_{1/4}$, $C = 1$, and $D = 4$. The adiabatically compressed dark matter haloes differ from the original NFW profiles, so we also fit the initial compressed halo profiles to equation (14) with $D = 3$.

The results are summarized in Table 2 and show an interesting trend: the density profiles of the dark matter haloes retain their shape to a remarkable degree throughout the merger. In fact, the main difference between the initial and final ρ_{dm} is an overall amplitude change by a factor of ~ 1.4 , regardless of the merger orbit or whether the halo is compressed. The bulges show more evolution after the mergers, especially in the inner slope of the density profile. In all cases the fitted inner slope of the bulge steepens noticeably. Although observations indicate that massive elliptical galaxies have surface brightness cores (Faber et al. 1997), the size of these cores tends to be ~ 100 pc (for the galaxy masses in our simulations). This scale is below our force softening of $\epsilon = 0.3$ kpc, so there is no inconsistency between our surface brightness or density profiles and observations of elliptical galaxies. As with the dark matter, the total profile for stars plus dark matter changes mostly by an overall amplitude and remains close to isothermal on the scale of R_e .

We also calculate the final virial radius of each dark matter halo and compare the enclosed mass M_v with the initial value in Table 2. In each case only about 65-70% of the initial virial mass ends up in the final virial radius; a similar ratio was found in our earlier study of dark-matter-only

mergers (Boylan-Kolchin & Ma 2004). This “puffing up” of the outer part of the dark matter halo is in stark contrast to the stellar bulge, where essentially all of the initial stellar mass M_* ends up in the final bulge. (This result is insensitive to changes in merger orbit, compression of halo, and the value of M_{dm}/M_* .) The ratio of the dark matter to stellar mass within the virial radius therefore decreases after a major collisionless merger. However, as discussed below in Section 3.5, the dark matter-to-stellar mass ratio within the central region of a galaxy (within R_e) shows the opposite behavior.

3.2 Remnant Shapes

We find that the merger remnants in our simulations tend to be triaxial, with their structure determined by the initial orbit: radial orbits produce nearly prolate remnants while orbits with non-zero angular momentum yield triaxial products.

To quantify this trend, we determine the axis ratios of the final products using an iterative eigenvalue technique (Dubinski & Carlberg 1991). We diagonalize a modified inertia tensor $I_{ij} = \sum x_i x_j / R^2$ (where $R^2 = x^2 + y^2/(b/a)^2 + z^2/(c/a)^2$ is the ellipsoidal radius of a particle and $a \geq b \geq c$ are the eigenvalues of I_{ij}) by first assuming spherical symmetry and computing I_{ij} , then using the eigenvalues of iteration n as input values for iteration $n + 1$. We also compare the axis ratios calculated both cumulatively ($r_i \leq R$) and in differential shells ($R_1 \leq r_i \leq R_2$). For the dark matter haloes, these two methods give similar results at most radii, but near r_v the cumulative method is less sensitive to local changes in the axis ratios due to the contribution of many particles at smaller radii, an effect noted previously in Kazantzidis et al. (2004). The cumulative method is, however, more robust for the bulges due to the relatively low number of stellar particles. For the following analysis we thus use the cumulative method for measuring the shapes of both components.

The top two panels of Figure 3 show the axis ratios of the remnant stellar bulges at $t = 6$ Gyr from four of our production runs (we do not include run N20 because its axis ratios are nearly indistinguishable from run M20). The radial orbit (dotted curves) results in a prolate bulge with both b/a and $c/a \approx 0.5$, irrespective of radius. The “most probable” orbit, on the other hand, yields a triaxial bulge

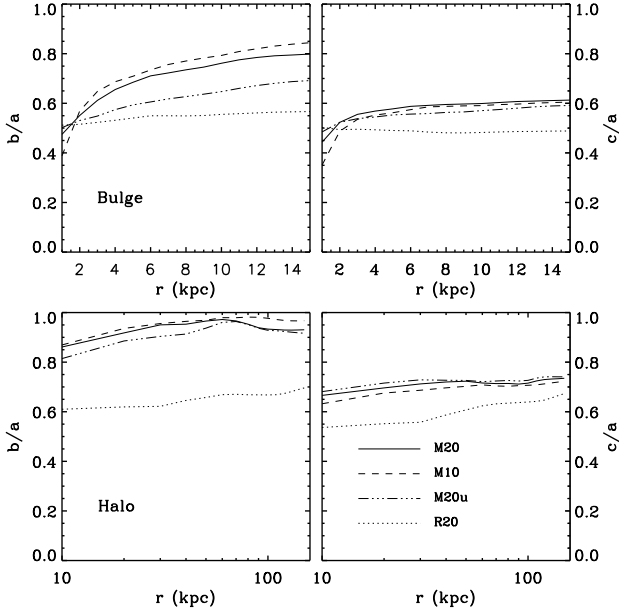


Figure 3. Triaxiality of the merged stellar bulges (top) and dark matter haloes (bottom) as a function of radius at $t = 6$ Gyr from four production runs. Axis ratios b/a (left) and c/a (right) are shown ($a \geq b \geq c$ by definition). Radial orbits (dotted curves) tend to produce prolate bulges and haloes, whereas orbits with non-zero angular momentum result in triaxial bulges and nearly oblate haloes. Note that the ratios for the bulge are plotted linearly in radius, while those for the halo are plotted logarithmically.

with axis ratios that have a mild radial dependence. These axis ratios are in agreement with a recent analysis of the SDSS data that found that bulges of early-type galaxies are consistent with triaxial ellipsoids (Vincent & Ryden 2005), though we note that Alam & Ryden (2002) also found that prolate ellipsoids are consistent with the SDSS early data release sample. Simulations of a brightest cluster galaxy from a cosmological simulation (Dubinski 1998) find a stellar remnant with $b/a = 0.66$, which is similar to our remnants of the “most probable” orbits, and $c/a = 0.47$, which is closer to what we find for a radial merger. The latter is a consequence of the correlated directions of Dubinski’s multiple mergers along filaments.

The bottom two panels of Figure 3 show the axis ratios for the merged dark matter haloes. The radial orbit again results in a mostly prolate halo, whereas the three “most probable” orbit runs give nearly oblate haloes with $b \approx a$ and $c/a \approx 0.7$, largely independent of M_{dm}/M_* and halo compression. It is useful to compare our results with those from dark-matter-only cosmological simulations of Bailin & Steinmetz (2004). For a fair comparison, we calculate the axis ratios of our remnants in a shell from 0.25 to $0.4r_v$, the same range as Bailin and Steinmetz use. We find the “most probable” orbit to give $b/a \approx 0.9 - 0.95$ and $c/a \approx 0.7$ while the radial orbit gives a remnant with $b/a \approx c/a \approx 0.7$. Both agree with the results of Jing & Suto (2002) and Bailin & Steinmetz (cf their fig. 5), though our values of b/a tend to be at the high end of their distribution.

The difference in the “most probable” orbit runs between the bulge (triaxial) and halo (oblate) shapes is note-

worthy, as it relates to the difference between the merging of the haloes and of the bulges. The haloes merge relatively quickly, but the bulges circle each other and spiral inward due to dynamical friction on the haloes. The final plunge of the bulge tends to be relatively radial even though the initial orbit has substantial angular momentum, giving the remnant bulge a different shape from the remnant haloes. Quantitatively, we find that the amount of (initial orbital) angular momentum lost from the bulge is $\sim 75\%$ (i.e. $\bar{L}_f \approx 0.25\bar{L}_i$). As a related measure, we calculated the ratio of rotation velocity to velocity dispersion for several projections. As might be expected, the maximal $v_{rot}/\sigma \approx 0.5$ at R_e occurs in the plane of the orbit, while for most lines of sight $v_{rot}/\sigma < 0.3$, typical of a slowly rotating, pressure-supported bulge. This is consistent with recent simulations by Naab & Burkert (2003), who found that equal mass mergers of disk galaxies tend to result in pressure-supported ellipticals while mergers with mass ratios of 3:1 and 4:1 result in oblate rotators (with $v_{rot}/\sigma > 0.7$).

3.3 The Fundamental Plane Relations

Before investigating the scaling relations among the effective radius R_e , velocity dispersion σ_e , and mass of the stellar bulge M_* , we first describe how we determine R_e and σ_e . Because the remnant bulges are triaxial, their observable properties depend on the angle from which the bulge is viewed. To quantify this effect, we calculate the properties of each of our remnant bulges for 10^4 random viewing angles. A standard technique for obtaining the effective radius is to fit the projected profile to a Sersic profile and use the derived R_e as the half-light radius. As described in Appendix A, however, we find this procedure does not give unique results, so we employ an alternate technique here. We calculate the surface mass density perpendicular to each line of sight in spherical bins as well as the projected enclosed mass at each radius. We define the projected radius of the particle enclosing half the total mass to be the half-light radius R_e . This procedure recovers the correct R_e for the initial Hernquist profile to within 1-2 %. For the velocity dispersion, we use the surface-brightness weighted dispersion within R_e ,

$$\sigma_e^2 \equiv \sigma_a^2(R_e) = \frac{\int_0^{R_e} \sigma_{los}^2(R) I(R) R dR}{\int_0^{R_e} I(R) R dR}, \quad (15)$$

where $I(R)$ is the surface brightness and σ_{los} is the line-of-sight velocity dispersion. Observationally, a commonly used definition is the dispersion measured within an aperture of size $R_e/8$. For our simulations, however, $R_e/8$ is comparable to the force softening ϵ , so we instead define our velocity dispersion within R_e . We do not expect this modification to bias our results with respect to observations because the aperture dispersion profile $\sigma_a(R)$ is generally quite flat within R_e (Gerhard et al. 2001). Any error introduced will almost certainly be less than that associated with empirically correcting the observed aperture dispersions to $R_e/8$. To be conservative with respect to force accuracy, we use 2ϵ as the minimum radius for the integral in equation (15).

Figure 4 shows the resulting distributions of R_e (top panels) and σ_e (middle panels) from 10^4 random viewing angles of our merger remnants from two simulations with different orbits: “most probable” (left panels) and radial

Table 3. Mean (left) and mode (right) of the distributions of the effective radius R_e and velocity dispersion σ_e from 10000 random projections of the remnant bulge in each of our five production runs. Parameters α and β are the resulting exponents for two projections of the fundamental plane relation: $R_e \propto M_*^\alpha$ and $M_* \propto \sigma_e^\beta$.

| Run | Mean | | | | Mode | | | |
|------|----------------|----------------------|----------|---------|----------------|----------------------|----------|---------|
| | R_e (kpc) | σ_e (km/s) | α | β | R_e (kpc) | σ_e (km/s) | α | β |
| M10 | 6.94 | 200.0 | 0.75 | 4.9 | 6.45 | 204.5 | 0.64 | 4.2 |
| M20 | 4.80 | 175.7 | 0.75 | 4.7 | 4.58 | 179.0 | 0.69 | 4.1 |
| N20 | 4.85 | 173.0 | 0.77 | 5.2 | 4.63 | 176.0 | 0.70 | 4.6 |
| M20u | 4.53 | 153.0 | 0.68 | 3.1 | 4.49 | 150.0 | 0.67 | 3.5 |
| R20 | 6.63 | 162.8 | 1.23 | 8.7 | 7.01 | 154.3 | 1.31 | 27 |

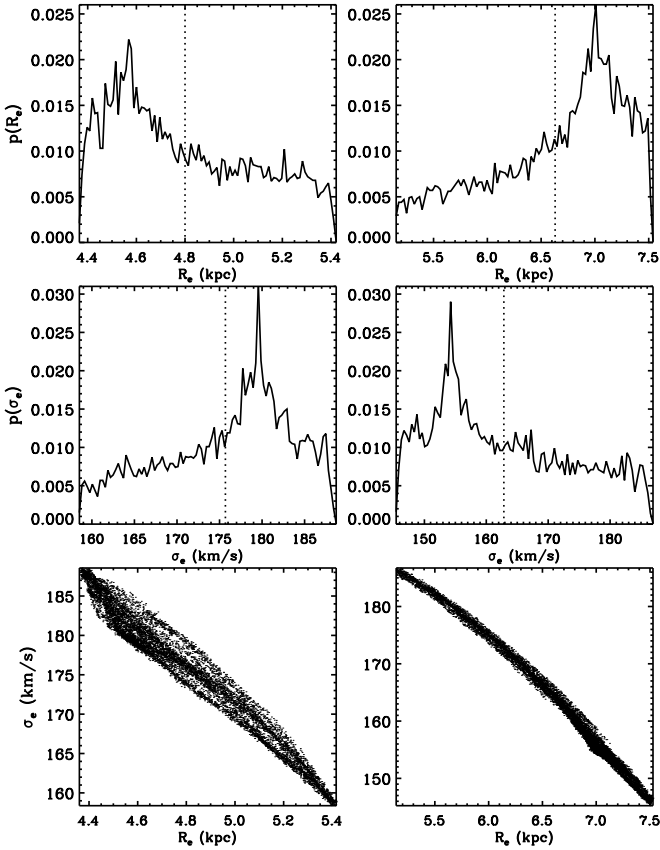


Figure 4. Distributions of R_e (top) and σ_e (middle), as well as the correlation at fixed mass between R_e and σ_e (bottom), for 10000 random viewings of the merged stellar bulge in runs with $M_{dm} = 20M_*$. Left: “most probable” orbit with $v_\theta/v_r \approx 0.7$ (run M20). Right: radial orbit (run R20). Note that the mean (dotted line) and mode can differ significantly, as the distributions are heavily skewed. The distributions are also dependent on orbit: for run M20 the mean R_e is greater than the mode and the mean σ_e is smaller than the mode, while the reverse holds for run R20. In both cases the “observed” R_e and σ_e are highly correlated, as indicated by the bottom two panels.

(right panels). The distributions are highly non-Gaussian, although in each case there is a reasonably well-defined mode that differs significantly from the mean (indicated by the vertical dotted line). The two orbits result in strikingly different distributions of R_e and σ_e . This difference is primarily because the two classes of orbits yield remnants with differ-

ent shapes (see Section 3.2 above). The “most probable” orbit yields a triaxial remnant for which one is more likely to observe a small R_e whereas the radial orbit yields a prolate remnant for which one is more likely to observe a large R_e . In addition, mergers on orbits with non-zero angular momentum (such as the “most probable” orbit) suffer more dynamical friction and thus more energy transfer from the stellar bulge to the dark matter (see also Section 3.4 and Table 4). This effect leads to a smaller and more tightly bound bulge with a larger velocity dispersion.

The bottom panels of Figure 4 show the correlation between the fundamental plane parameters R_e and σ_e for fixed stellar mass from the 10^4 viewing angles. It is evident that the measurements are highly correlated; viewing angles that yield a relatively small effective radius result in a relatively large velocity dispersion. This effect is due to projection: looking down the major axis of a prolate remnant, for example, leads to a smaller effective radius and larger velocity dispersion than if the viewing angle is along a minor axis. These correlations are also expected from the fundamental plane at fixed luminosity (or mass): from the SDSS values for equation (1), $R_e \propto \sigma_e^{-3}$ at fixed luminosity. Although the fundamental plane cuts through the $R_e - \sigma_e$ plane in a non-trivial manner, making a direct comparison between the spread in our $R_e - \sigma_e$ correlations and the scatter of the fundamental plane difficult, the thickness of the correlations we present here are consistent with the observed small scatter in the fundamental plane. However, it is not clear how additional effects, such as scatter in the global M_{dm}/M_* and in initial sizes and shapes of merging galaxies, would affect this scatter.

Using the results of Figure 4, we can now assess the extent to which the stellar bulges remain on the projections of the fundamental plane after major dissipationless mergers. Table 3 lists the mean and mode of R_e and σ_e for the merged stellar bulges and the slopes for power-law fits to $R_e - M_*$ and $M_* - \sigma_e$ from our five production runs. Since the mean and modes differ significantly, we present results for each definition of the “average” remnant. The results for $R_e - M_*$ shown in Table 3 are more robust than those for $M_* - \sigma_e$ because of the steepness of the latter relation.

Table 3 shows that for the “most probable” orbit with adiabatically compressed dark matter haloes (i.e. runs “M10” and “M20”, which are the best motivated models studied in this paper), the derived fundamental plane slopes using the mode are reasonably consistent with observations:

$$R_e \propto M_*^\alpha, \quad \alpha = 0.64 - 0.69,$$

Table 4. Parameters from the bulge energy conservation equation (eqn. 18) derived from the simulations. We quote numbers for the remnant bulge structural parameter f_f using both the mean R_e and mode R_e obtained from 10^4 random projections (listed in Table 3). Parameters f_{orb} and f_t characterize the initial orbital energy (at virial radius) and the energy transfer between the stellar and dark matter components due to mergers.

| Run | f_i | $f_{f,mean}$ | $f_{f,mode}$ | f_{orb} | f_t |
|------|-------|--------------|--------------|-----------|-------|
| M10 | 0.342 | 0.385 | 0.358 | 0.118 | 0.344 |
| M20 | 0.367 | 0.444 | 0.424 | 0.144 | 0.469 |
| N20 | 0.367 | 0.448 | 0.428 | 0.215 | 0.394 |
| M20u | 0.265 | 0.319 | 0.316 | 0.144 | 0.375 |
| R20 | 0.367 | 0.489 | 0.517 | 0.00715 | 0.183 |

$$M_* \propto \sigma_e^\beta, \quad \beta = 4.1 - 4.2. \quad (16)$$

Recall that the initial values of R_e , M_* , and σ_e for these simulations also lie on the fundamental plane (see Section 2.2). In comparison, the “most probable orbit” model with an *uncompressed* dark matter halo (run “M20u”) produces a $M_* - \sigma_e$ relation somewhat shallower than the observed relation, while radial orbits (run “R20”) yield a remnant well off the fundamental plane ($\beta \sim 27!$). In fact, the remnant from the head-on merger is much further off the fundamental plane than the intrinsic scatter of the plane, suggesting that few major mergers are radial or nearly so. This inference is consistent with the low frequency of head-on mergers in the orbital analyses discussed in Section 2.2.

3.4 Homology and Energy Conservation

Semi-analytic galaxy formation models often use energy conservation arguments and rely on the assumption of homology for predicting how elliptical galaxies evolve during dissipationless mergers (Cole et al. 2000; Shen et al. 2003). The energy conservation equation is usually derived using the fact that on dimensional grounds we can quantify the energy of a single bulge of mass M_* as

$$E \equiv -f \frac{GM_*^2}{R_*} \quad (17)$$

for some characteristic radius R_* and structural parameter f that depends on the properties of the galaxy model under consideration. For a bulge with the Hernquist profile (without a dark matter halo), $E = -GM_*^2/12a$, so $f = R_e/12a = 0.151$ using $R_* = R_e$, or $f = (1 + \sqrt{2})/12 = 0.201$ using $R_* = r_{1/2}$. For our various bulge-plus-halo models, we find $f = 0.265 - 0.367$ (see Table 4) due to the presence of a dark matter halo.

Using equation (17), we can write an energy conservation equation for the bulges in a binary merger of two galaxies (with initial bulge masses M_1 and M_2) as

$$f_f \frac{M_f^2}{R_f} = f_1 \frac{M_1^2}{R_1} + f_2 \frac{M_2^2}{R_2} + (f_{orb} + f_t) \frac{M_1 M_2}{R_1 + R_2}, \quad (18)$$

where f_{orb} contains information about the orbital energy and f_t describes the energy transfer between the stellar and dark matter components. With this definition, $f_t > 0$ implies that the final bulge is more tightly bound than the initial bulges, i.e. energy is transferred from the bulge to the dark

matter halo. (An equation analogous to equation (18) can be used to describe the dark matter component.) As noted by previous authors, setting $f_f = f_1 = f_2$ and $f_{orb} = f_t = 0$ (i.e., perfect homology and a parabolic orbit with no energy transfer between the dark matter and the stellar component) implies $R \propto M_*$ for an equal mass merger, which does not match the observed relation. Alternatively, assuming homology is satisfied ($f_f = f_i$) and $R \propto M_*^\alpha$, one can derive that

$$\frac{f_{orb} + f_t}{f_i} = \left(\frac{\xi^\alpha + 1}{\xi} \right) [(\xi + 1)^{2-\alpha} - \xi^{2-\alpha} - 1]. \quad (19)$$

for binary mergers between galaxies with mass ratio ξ . The observed $R_e - M_*$ relation is $\alpha = 0.56$, implying $f_{orb} + f_t = 1.43f_i$ for equal-mass mergers if homology is satisfied.

To assess homology in our simulations we calculate the values of f using the energy defined in Appendix B:

$$E = \sum_i \left(\frac{1}{2} m_i v_i^2 - \sum_{j>i} \frac{G m_i m_j}{r_{ij}} - \sum_k G m_i m_k \frac{\vec{r}_i \cdot \vec{r}_{ik}}{r_{ik}^3} \right) \quad (20)$$

where $r_{ij} \equiv |\vec{r}_i - \vec{r}_j|$ and i and j run over all stellar particles while k runs over all dark matter particles. The resulting values for f are shown in Table 4. Homology is preserved at the $\sim 15\%$ level in all three runs with the “most probable orbit” (runs M10, M20, and M20u): f increases slightly in these runs, with the mean value changing more than the mode, but in each run both values are within 20% of the initial value. The same is true for run N20, which is identical to M20 aside from having lower orbital velocity. The radial merger (run R20), however, breaks homology significantly more than the “most probable” orbit. In all five production runs, the ratio of bulge-dark matter to bulge-bulge potential energy increases, reflecting the relative distribution of dark matter and stars, a point which we discuss further in Section 3.5.

Table 4 also gives the values of f_{orb} and f_t , the parameters characterizing the amount of initial orbital energy (at the virial radius) and the amount of energy transferred between the stellar and dark components. For the “most probable” orbit, $f_t \approx 0.34 - 0.47$, indicating that there is a significant amount of energy lost from the stellar bulge to the dark matter halo during the merger (partially via dynamical friction). The energy transfer is significantly less for the head-on merger in which dynamical friction is less important. The values of $(f_t + f_{orb})/f_i \approx 1.3 - 1.7$ for the most probable orbit are reasonably consistent with the estimate above for the amount of energy transfer required to explain the observed $R_e - M_*$ relation. Interestingly, a comparison of run N20 to M20 show that while N20 has less orbital energy, it also less energy transferred from the bulge to halo and the net result is a halo with nearly identical homology properties to those from run M20.

3.5 The Dark Matter Fraction

As noted in Section 1, the fundamental plane relations are tilted from the simple one-component predictions based on the virial theorem. One possible explanation for the origin of this tilt is a luminosity-dependent dark matter fraction within the effective radius. In this section we test this hypothesis by quantifying how the dark matter fraction evolves during our simulations.

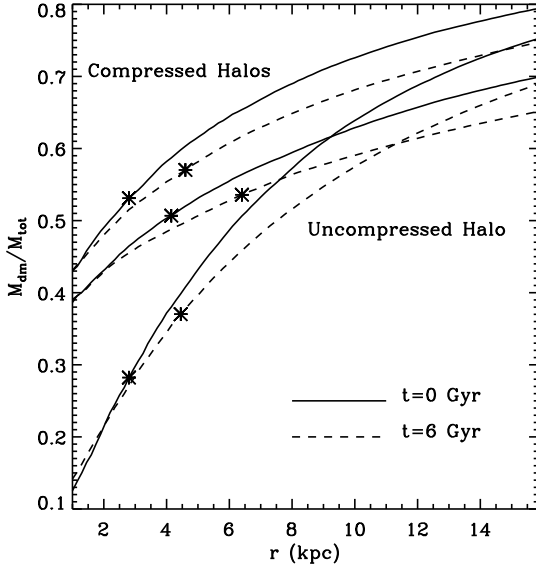


Figure 5. Ratio of dark matter mass to total mass interior to radius r as a function of r for initial condition (solid curve) and remnant system (dashed curve) for simulation M20 (compressed halo; upper curves), M10 (compressed halo; middle curves), and M20u (uncompressed halo; lower curves). The symbols mark the effective radius R_e for the given simulation. In each case the fraction of dark matter interior to R_e increases after the merger.

In Figure 5 we plot the ratio of dark matter mass to total mass $M_{dm}(< r)/M_{tot}(< r)$ as a function of radius for the three simulations using the “most probable” orbit: runs M20 (upper curves) and M10 (middle curves) have compressed dark matter halos while run M20u (lower curves) has a standard NFW halo. Both the initial (solid curves) and remnant (dashed curves) galaxies are shown and the mode effective radius R_e of each model’s bulge is marked with an asterisk. The results for the initial models (solid lines) show the dramatic effect of adiabatic contraction in the inner region of a galaxy: the dark matter mass interior to R_e in the adiabatically contracted model is approximately twice that of an uncompressed NFW halo. After the merger the dark matter fraction interior to a given radius decreases, but the dark matter fraction interior to the final R_e is *greater* than the dark matter fraction interior to the initial R_e for both simulations. This increasing dark matter fraction with stellar mass is consistent with that needed to explain the observed tilt in the fundamental plane. Quantitatively, we find $M_{dyn} \propto M_*^{1.11}$ for the compressed haloes and $M_{dyn} \propto M_*^{1.19}$ for the uncompressed haloes. These results are reasonably consistent with the observational results of Padmanabhan et al. (2004) from SDSS. The amount of dark matter within R_e can be constrained in other ways, particularly through gravitational lensing. Though a large, statistically significant sample of lenses is needed, the dark matter fraction we obtain is consistent with analyses of existing lensing observations (e.g. Treu & Koopmans 2004; Rusin & Kochanek 2005).

One way to understand the increasing dark matter fraction is based on the dark matter mass profile in the inner parts of the galaxy: assume that the dark matter mass

profile is given by $M_{dm}(r) \propto M_v r^\eta$. For an NFW profile, $\eta \approx 2$ at the small radii appropriate near R_e . For an adiabatically compressed halo, $\eta \approx 1.2$ (Table 2). If the bulge stays roughly on the $R_e - M_*$ relation, R_e increases by a factor of ≈ 1.5 during an equal-mass merger. The stellar mass within R_e increases by a factor of 2 during such a merger, while the dark matter mass within R_e increases by a factor of $\approx 2 * 1.5^\eta \approx 3.25 - 4.5$ if the virial mass also doubles. If the final virial mass is only a factor of ≈ 1.3 of the initial virial mass (Table 2), the dark matter mass within R_e increases by a smaller factor of $\approx 1.3 * 1.5^\eta \approx 2.1 - 3$. All of these estimates yield a dark matter fraction within R_e that increases after the merger, consistent with our simulations.

4 SUMMARY & DISCUSSION

We have performed numerical simulations of dissipationless mergers of equal-mass galaxies containing a stellar bulge and a dark matter halo to study how observable properties of elliptical galaxies scale during mergers. Some key features of our simulations include:

- We consider both standard NFW dark matter haloes and NFW haloes modified by adiabatic response to baryonic dissipation.
- We set up the initial stellar bulges using the observed $R_e - M_*$ projection of the fundamental plane (most of which also follow the observed $M_* - \sigma_e$ relation).
- Our primary merger orbit is taken from the most probable value of a cosmological distribution, which is weakly bound with $v_\theta \approx 0.7 v_r$. We also simulate a merger on a radial parabolic orbit and a merger on an orbit with the initial orbital velocities reduced by 15% for comparison.
- We perform a large number of random projections of each merger remnant in order to determine the effects of viewing angle on the observable characteristics.
- Our resolution tests indicate that $\sim 5 \times 10^5$ dark matter particles per halo are necessary to accurately resolve the dynamics of the stellar component on the scale corresponding to observations. Test runs with a smaller number of particles lead to artificially “puffed up” stellar remnants.

The main results of our work are:

- As in previous studies, we find that the remnant bulges retain a de Vaucouleurs profile. In addition, the spherically-averaged radial density profiles of the dark matter haloes appear to be scaled-up versions of those of their progenitors, i.e., with the dark matter density increasing by a simple normalization factor.
- The remnant shapes depend strongly on the orbit of the merger. The cosmologically “most probable” orbit results in a nearly oblate halo with a triaxial bulge, while less probable radial orbits result in prolate bulges and haloes.
- The $R_e - M_*$ and $M_* - \sigma_e$ projections of the fundamental plane are roughly preserved for an “average” viewing angle in major dissipationless mergers with the most probable orbit, independent of the global ratio of dark to luminous matter (Table 3). There are, however, significant variations with viewing angle, and the observables are strongly correlated (Fig. 4). The viewing-angle scatter appears consistent with the observed scatter in the fundamental plane. Our

simulations thus suggest that the fundamental plane is consistent with models in which massive elliptical galaxies undergo significant growth via late dissipationless mergers. If the merging elliptical galaxies contain central massive black holes, and if black hole masses roughly add when they coalesce (i.e., there is not significant energy loss to gravitational waves), then our results also imply that dissipationless mergers maintain the $M_{\text{BH}} - \sigma_e$ (Gebhardt et al. 2000; Ferrarese & Merritt 2000) and $M_{\text{BH}} - M_*$ (Magorrian et al. 1998; Häring & Rix 2004) relations.

- The merger remnants contain more dark matter (relative to stellar matter) within R_e than their progenitors: $M_{\text{dyn}} \propto M_*^{1.11-1.19}$, consistent with the hypothesis that the tilt of the fundamental plane is due to an increasing dark matter fraction within R_e .

- An appreciable amount of energy and angular momentum are transferred from the stars to the dark matter in the merging process. Quantitatively, the energy transfer found in our simulations is similar to that needed in semi-analytic galaxy formation models to explain the fundamental plane.

One important goal of studies of elliptical galaxies is to understand the origin of the tilt in the fundamental plane. The virial theorem expectation relates the stellar velocity dispersion and effective radius to the *total* mass within R_e : $\sigma_e^2 \propto M_{\text{dyn}}(< R_e)/R_e$. The fundamental plane relates stellar velocity dispersion, luminosity, and effective radius: $R_e \propto \sigma_e^{-3} L^{3/2}$. As discussed below equation (7), if metallicity or stellar age differences are solely responsible for the fundamental plane tilt then $M_{\text{dyn}} \propto M_*$ and $M_* \propto L^x$ with $x \approx 1.15$. On the other hand, if dark matter fraction is responsible, then $M_* \propto L$ and $M_{\text{dyn}} \propto M_*^x$ with $x \approx 1.15$. Our simulations contain no star formation or metallicity information and thus $M_* \propto L$ by assumption; we therefore do not have a direct way to evaluate the importance of metallicity variations (though we note that there is observational evidence for them; e.g. Trager et al. 2000; Cappellari et al. 2005). Nevertheless, we find that because of a change in the amount of dark matter with R_e due to a merger, dissipationless (major) mergers move elliptical galaxies roughly along the fundamental plane. It is interesting to note that the nearly homologous nature of the bulges in our simulations indicates that our results may hold for unequal mass mergers as well: using mass ratio $\xi = \frac{1}{3}$ rather than $\xi = 1$ results in only a 1% change in $(f_{\text{orb}} + f_t)/f_i$ from equation (19).

Because our simulations involve only gravitational interactions, the results can be interpreted at different mass and length scales by an appropriate rescaling of time. This is somewhat complicated in two-component simulations such as ours, however, because bulges and dark matter haloes do not scale in the same manner: for example, $R_e \propto M_*^{0.56}$ while $r_v \propto M_v^{0.33}$. If we rescale the length and mass according to the virial theorem definition, then the bulge no longer lies on the fundamental plane. For example, consider a mass scale 10 times larger than what is presented in this work (keeping the concentration constant). Both the virial radius and effective radius increase by a factor of $10^{1/3}$; then for run M20, the bulge effective radius will be $R_e = 10^{1/3} \times 2.81 \text{ kpc} = 6.05 \text{ kpc}$ rather than the 10.24 kpc predicted by the SDSS scaling (equation 13). This difference is comparable to the $1 - \sigma$ scatter Shen et al. find in the $R_e - M_*$ relation. As a result, we can indeed scale

our simulations up or down by a factor of 10 in mass and $10^{1/3}$ in radius and still be near the fundamental plane. Since the rescaling only affects the amplitude of the relations, the slopes in equation (16) and Table 3 are actually preserved and the scaled mergers would move along the fundamental plane but with a constant offset.

The results of Section 3.2 show that our remnant bulges are either triaxial (non-radial orbit) or prolate (radial orbit), in agreement with analyses of SDSS data. In this context it is important to point out that our initial conditions are spherical and isotropic, while both the remnants of our mergers and observed ellipticals tend to be triaxial. It would certainly be desirable to use more realistic (i.e. non-spherical) initial conditions in future work, though there are significant difficulties in doing so: operationally, it is not possible to create stable triaxial initial conditions corresponding to a desired density profile. It would also be of interest to extend the results presented here by including a gaseous or stellar disk. Such simulations should help shed light on the origins of both spheroidal systems and the fundamental plane, topics that we have not addressed in this work. We note that in simulations of mergers of halo-bulge-disk systems performed by Barnes (1992), the stellar remnant followed a similar radius-mass relation ($r \propto M^{0.5}$) to what we find for halo-bulge mergers, perhaps implying that inclusion of a collisionless stellar disk would not change the conclusions of this work drastically, but this issue must be resolved with future simulations.

ACKNOWLEDGMENTS

We thank A. Dekel, S. Faber, L. Hernquist, N. Murray, & T. Thompson for useful discussions and Volker Springel for making GADGET available. This research used resources of the National Energy Research Scientific Computing Center, which is supported by the Office of Science of the U.S. Department of Energy. CPM is partially supported by NSF grant AST 0407351 and NASA grant NAG5-12173. EQ is supported in part by NSF grant AST 0206006, NASA grant NAG5-12043, an Alfred P. Sloan Fellowship, and the David and Lucile Packard Foundation.

REFERENCES

- Alam S. M. K., Ryden B. S. 2002, ApJ, 570, 610
- Bailin J., Steinmetz M., 2005, ApJ submitted (astro-ph/0408163)
- Barnes J. E. 1992, ApJ, 393, 484
- Barnes J. E., Hernquist L. 1992, ARA&A, 30, 705
- Benson A. J. 2005, MNRAS, 358, 551
- Bernardi M. et al., 2003a, AJ, 125, 1849
- Bernardi M. et al., 2003b, AJ, 125, 1866
- Binney J., Tremaine S. 1987, Galactic Dynamics, Princeton University Press, Princeton, N. J.
- Blanton M. et al 2005, ApJ in press (astro-ph/0310453)
- Blumenthal G. R., Faber S. M., Flores R., Primack J. R. 1986, ApJ, 301, 27
- Borriello A., Salucci P., Danese L. 2003, MNRAS, 341, 1109
- Boylan-Kolchin M., Ma C.-P., 2004, MNRAS, 349, 1117

- Burkert A., Naab T. 2003, in “Galaxies and Chaos”, eds. G. Contopoulos and N. Voglis (Springer); astro-ph/0301385
- Capelato H. V., de Carvalho R. R., Carlberg R. G. 1995, ApJ, 451, 525
- Cappellari M. et al., MNRAS submitted (astro-ph/0505042)
- Ciotti L., Bertin G. 1999, A & A, 352, 447
- Cole S., Lacey C. G., Baugh C. M., Frenk C. S. 2000, MNRAS, 319, 168
- Dantas C. C., Capelato H. V., Ribeiro A. L. B., de Carvalho R. R. 2003, MNRAS 340, 398
- de Vaucouleurs G. 1948, Ann. d’Astrophys., 11, 247
- Dehnen W. 1993, MNRAS, 265, 250
- Djorgovski S., Davis M. 1987, ApJ, 313, 59
- Dressler A., Lynden-Bell D., Burstein D., Davies R. L., Faber S. M., Terlevich R. J., Wegner G. 1987, ApJ, 313, 42
- Dubinski J. 1998, ApJ, 502, 141
- Dubinski J., Carlberg R. G. 1991, ApJ, 378, 496
- Faber S. M., Jackson R. E., 1976, ApJ, 204, 668
- Faber S. M., Tremaine S., Ajhar E. A., Byun Y. I., Dressler A., Gebhardt K., Grillmair C., Kormendy J., Lauer T. R., Richstone D. 1997, AJ 114, 1771
- Ferrarese L., Merritt, D. 2000, ApJ, 539, L9
- Gao L., Loeb A., Peebles P. J. E., White S. D. M., Jenkins A. 2004, ApJ, 614, 17
- Gebhardt K. et al., ApJ, 539, L13
- Gerhard O., Kronawitter A., Saglia R. P., Bender R. 2001, AJ, 121, 1936
- Gnedin O. Y., Kravtsov A. V., Klypin A. A., Nagai D. 2004, ApJ, 616, 16
- González-García A. C., van Albada T. S. 2003, MNRAS, 342, L36
- Graham A., Colless M. 1997, MNRAS, 287, 221
- Häring N., Rix H.-W. 2004, ApJ, 604, L89
- Hernquist L. 1990, ApJ, 356, 359
- Jing Y. P. & Suto Y. 2002, ApJ, 574, 538
- Jorgensen I., Franx M., Kjaergaard P. 1996, MNRAS, 280, 167
- Kauffmann G. et al. 2003, MNRAS 341, 33
- Kazantzidis S., Kravtsov A. V., Zentner A. R., Allgood B., Nagai D., & Moore B. 2004, ApJ, 611, L73
- Kazantzidis S., Magorrian J., Moore B. 2004, ApJ 601, 37
- Khochfar S., Burkert A. 2003, ApJ, 597, L117
- Khochfar S., Burkert A. 2005, submitted to MNRAS (astro-ph/0309611)
- Magorrian J. et al. 1998, AJ, 115, 2285
- Moore B., Kazantzidis S., Diemand J., Stadel J. 2004, MNRAS, 354, 522
- Naab T., Burkert A. 2003, ApJ, 597, 893
- Navarro J. F., Frenk C. S., White S. D. M. 1997, ApJ, 490, 493
- Nipoti C., Londrillo P., Ciotti L. 2003, MNRAS, 342, 501
- Padmanabhan N. et al. 2004, New Astronomy, 9, 329
- Pahre M. A., de Carvalho R. R., Djorgovski S. G. 1998, AJ, 116, 1591
- Pahre M. A., de Carvalho R. R., Djorgovski S. G. 1998, AJ, 116, 1606
- Rusin D., Kochanek C. S. 2005, ApJ, 623, 666
- Seljak U. 2002, MNRAS, 334, 797
- Sersic J. L., 1968, Atlas de Galaxies Australes. Observatorio Astronomico, Cordoba
- Shen S., Mo H. J., White S. D. M., Blanton M. R., Kauffmann G., Voges W., Brinkmann J., Csabai I. 2003, MNRAS, 343, 978
- Springel V., Hernquist L. 2005, ApJ, 622, L9
- Springel V., White S. D. M. 1999, MNRAS, 307, 162
- Springel V., Yoshida N., White S. D. M. 2001, New Astronomy, 6, 79
- Steinmetz M., Navarro J. F. 2002, New Astronomy, 7, 155
- Tormen G. 1997, MNRAS, 290, 411
- Trager S. C., Faber S. M., Worthey G., González J. 2000, AJ, 120, 165
- Tremaine S., Richstone D. O., Byun Y., Dressler A., Faber S. M., Grillmair C., Kormendy J., Lauer T. R., 1994, AJ, 107, 634
- Treu T., Koopmans L. V. E. 2004, ApJ, 611, 739
- Toomre A., Toomre J. 1972, ApJ, 178, 623
- van Dokkum P. G., Franx M., Fabricant D., Kelson D. D., Illingworth G. D., 1999, ApJ, 520, L95
- Vincent R. A., Ryden B. S. 2005, ApJ, 623, 137
- Zentner A., Berlind A. A., Bullock J. S., Kravtsov A. V., Wechsler R. H. 2005, ApJ, 624, 505

APPENDIX A: SERSIC FITTING

A common parameterization of the surface brightness profile of a galaxy is that of Sersic (1968):

$$I(R) = I(R_e) \exp\{-b(m)[(R/R_e)^{1/m} - 1]\}. \quad (\text{A1})$$

Though the function $b(m)$ cannot be expressed in closed form, an accurate asymptotic expansion is given by Ciotti & Bertin (1999) as $b(m) \approx 2m - 1/3 + 4/(405m)$; bulges and early-type galaxies are typically well-approximated by the de Vaucouleurs (1948) law of $m = 4$. Fitting an observed surface brightness distribution to a Sersic profile is a standard technique for determining the (projected) half-mass radius R_e of a galaxy. We find that fitting our projected density profiles to Sersic profiles is not robust, however: changing the radial range of the fit leads to systematic variations in both the Sersic index and the corresponding effective radius.

This dependence of fitting results on the range of radii can be seen for the initial bulge that is assigned a Hernquist profile. Fig. A1 shows the derived R_e (top panel) and m (bottom panel) for an input Hernquist profile with $R_e = 2.81$ kpc as a function of the maximum radius of the fit. Two different values for the minimum radius of the fit are plotted: 0.1 kpc (X symbols) and 0.35 kpc (square symbols). In both cases the recovered R_e and m are increasing functions of the maximum radius of the fit; additionally, the recovered R_e is lower than the input $R_e = 2.81$ kpc and the Sersic index m is less than 4 for all reasonable maximum values of the fit. This result is not unexpected since Hernquist models deviate from the de Vaucouleurs profile at both small and large radii, but it does present a problem for quantitatively characterizing the stellar bulges in our simulations since the fitted R_e for the initial Hernquist profile can change by 20% or more depending on the range of radii considered; the final bulges show similar trends. In fact, Blanton et al. (2005) cite

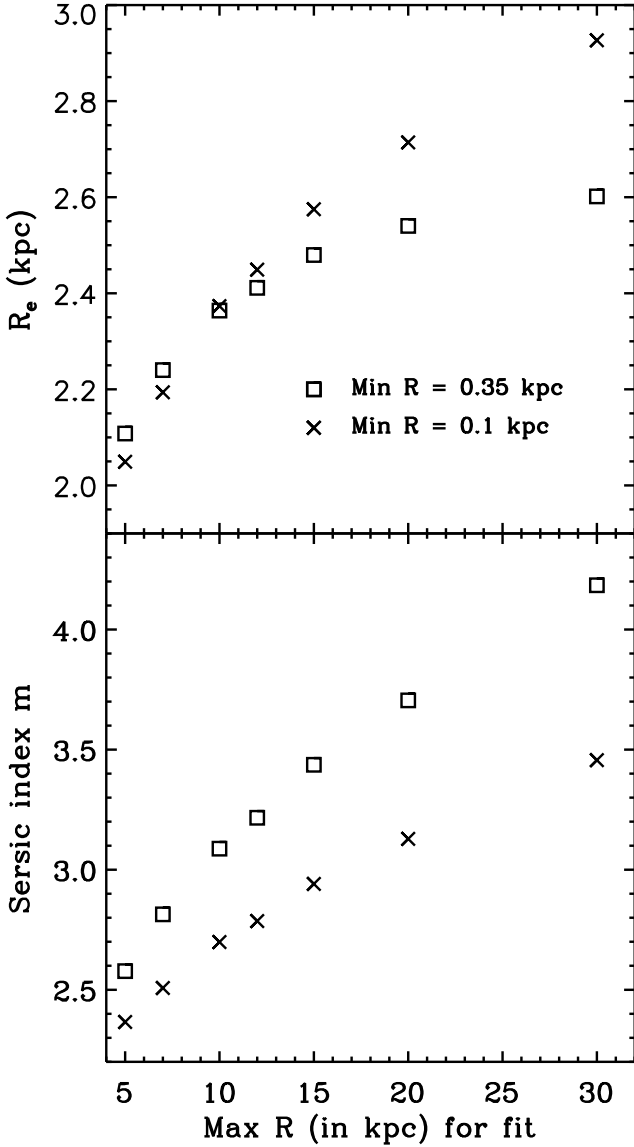


Figure A1. A demonstration of the dependence of R_e and m obtained from Sersic fitting (equation A1) on the radial range of the fit for a Hernquist profile with $R_e = 2.81$ kpc. The top panel plots the derived effective radius R_e as a function of the maximum radius to which the fit is performed while the bottom panel plots the fitted Sersic index m . The best-fit values of both R_e and m depend sensitively on both the maximum (horizontal axis) and minimum (symbols) radii used in the fit.

a similar issue with Sersic fits to SDSS observations (see their appendix A and fig. 10).

As a result, we do not use Sersic fits to determine the effective radii of either our initial conditions or merged ellipsoids. Instead, we take a line of sight and calculate the surface mass density perpendicular to the line of sight in spherical bins. We also calculate the projected enclosed mass at each radius. We define the projected radius of the particle enclosing half the total mass to be the half-light radius

(R_e). This procedure recovers the correct R_e for the initial hernquist profile to within 1-2 %.

APPENDIX B: ENERGY CONSERVATION

Consider a system of particles with distribution function f obeying the collisionless Boltzmann equation

$$\frac{\partial f}{\partial t} + \vec{v} \cdot \frac{\partial f}{\partial \vec{x}} - \frac{\partial \Phi}{\partial \vec{x}} \cdot \frac{\partial f}{\partial \vec{v}} = 0. \quad (\text{B1})$$

By taking, in turn, a velocity and spatial moment of equation (B1) we can obtain the tensor virial theorem (Binney & Tremaine 1987, sec. 4.3):

$$\frac{1}{2} \frac{d^2 I_{\alpha\beta}}{dt^2} = 2K_{\alpha\beta} + W_{\alpha\beta}, \quad (\text{B2})$$

where

$$I_{\alpha\beta} = \int \rho x_\alpha x_\beta d^3x, \quad (\text{B3})$$

$$K_{\alpha\beta} = \frac{1}{2} \int \rho \overline{v_\alpha v_\beta} d^3x, \quad (\text{B4})$$

$$W_{\alpha\beta} = - \int \rho x_\beta \frac{\partial \Phi}{\partial x_\alpha} d^3x \quad (\text{B5})$$

and $\overline{v_\alpha v_\beta}$ is the mean of $v_\alpha v_\beta$. For a steady-state system, the second derivative of the inertia tensor $I_{\alpha\beta}$ vanishes and the trace of equation (B2) gives the standard scalar virial theorem $2K = -W$. If we consider a system with a bulge (b) and dark matter (d), each with a distribution function obeying the collisionless Boltzmann equation with respect to the combined potential³, we can write the same tensor virial theorem for each component by replacing the total mass density ρ with the mass density of that component. This modification is straightforward for the inertia tensor and kinetic term but is somewhat more subtle for the potential term $W_{\alpha\beta}$. By writing the potential as the sum of the potential of each subsystem, $\Phi = \Phi_b + \Phi_d$, the trace for the bulge breaks into two separate parts:

$$W_b = - \int \rho_b \vec{x} \cdot \frac{\partial \Phi_b}{\partial \vec{x}} d^3x - \int \rho_b \vec{x} \cdot \frac{\partial \Phi_d}{\partial \vec{x}} d^3x. \quad (\text{B6})$$

The first term in the above equation, which we denote W_{bb} , is the familiar self-energy of the bulge. The second term, W_{bd} , describes the interaction energy of the bulge with the dark matter halo. If we write the mass density as a sum over (Dirac) delta functions

$$\rho_b = \sum_{i \in b} m_i \delta(\vec{x} - \vec{x}_i) \quad (\text{B7})$$

and similarly for component d , then this term takes a more transparent form:

$$W_{bd} = - \sum_{i \in b} \sum_{j \in d} G m_i m_j \frac{\vec{x}_i \cdot (\vec{x}_i - \vec{x}_j)}{|\vec{x}_i - \vec{x}_j|^3}. \quad (\text{B8})$$

This quantity W_{bd} is energy belonging to the bulge due to the interaction of the bulge with the dark matter such

³ Since phase space densities are additive, the total phase space density $f_{tot} = f_b + f_d$ also obeys the collisionless Boltzmann equation.

that the total potential energy of the bulge is defined as $W_b \equiv W_{bb} + W_{bd}$. [The second term in equation (20) is W_{bb} while the third term is W_{bd} .] We similarly define the total potential energy of the dark matter halo to be $W_d \equiv W_{dd} + W_{db}$. Note with this definition we have

$$W_{bd} + W_{db} = - \sum_{i \in b} \sum_{j \in d} G m_i m_j \frac{1}{|\vec{x}_i - \vec{x}_j|}, \quad (\text{B9})$$

which is simply the “cross” potential energy of the bulge and dark matter components, and thus

$$W_b + W_d = W_{bb} + W_{bd} + W_{dd} + W_{db} = W_{\text{tot}} \quad (\text{B10})$$

where W_{tot} is the total potential energy of the system. For each galaxy used in our initial conditions, $2 T_{bb}/|W_{bb} + W_{bd}| = 1$ to within 1%.